Chloride adsorption at the Au(111) electrode surface

Zhichao Shi, Jacek Lipkowski

Guelph-Waterloo Center for Graduate Work in Chemistry, Guelph Campus, University of Guelph, Guelph, Ont. N1G 2W1, Canada

Received 24 July 1995

Abstract

A thermodynamic analysis of charge density data was performed to describe chloride adsorption at the Au(111) electrode surface. The Gibbs excess, the Gibbs energy of adsorption, the number of electrons flowing to the interface per adsorbed chloride ion at a constant potential (electrosorption valency) and a constant chloride concentration (reciprocal of the Esin–Markov coefficient), and the dipole formed by adsorbed ion and its image charge in the metal were determined. Chloride forms a chemisorption bond with gold whose polarity is a strong function of the charge on the metal. The bond is fairly polar at the negatively charged surface; however its polarity drops significantly at positive charges. The adsorption behavior of this anion is asymmetric with respect to the charge on the metal.

Keywords: Electroadsorption; Surface chemistry; Chloride; Au(111) electrode

1. Introduction

The aim of this paper is to provide a thermodynamic analysis of recent charge density data which describe chloride adsorption at the Au(111) electrode surface [1]. Chloride adsorption at Au(111) was investigated qualitatively by means of differential capacity [2] and cyclic voltammetry [3] and quantitatively by chronocoulometry [1] and surface X-ray scattering [4]. In this paper we describe the energetics of Cl^- adsorption at the Au(111) electrode and provide thermodynamic data such as adsorption isotherms, Gibbs energies of adsorption and electrosorption valencies. We also evaluate the dipole moment formed by the adsorbed Cl^- ion and its image charge in the metal and discuss the impact of Cl^- adsorption on the interface structure.

2. Experimental

The methods and procedures have been described in the preceding papers [1,5–8], and we repeat only the main points here. The gold single-crystal electrode was flame annealed before experiments. The counter-electrode was a gold coil. The reference electrode was an external saturated calomel electrode (SCE) connected to the cell through a salt bridge.

Two series of measurements were carried out. The measurements for series 1 were conducted in 0.1 M $KClO_4$ + x M KCl and covered the potential range from -0.8 to $+0.6$ V/SCE. The measurements for series 2 were performed in 0.1 M $KClO_4$ + 10^{-3} M $HClO_4$ + x M KCl to extend the positive limit of potentials from $+0.6$ to $+0.8$ V/SCE. The concentration of KCl varied between 5×10^{-6} and 5×10^{-3} M in these studies. Water was purified in a Millipore system (resistivity > 18 MΩ cm). Potassium perchlorate was purified as described previously [8]. Perchloric acid (Aldrich Chemical Company, 99.999%) and potassium chloride (Alfa Johnson Matthey Ltd., 99.999%) were used without further purification. All solutions were deaerated with argon, and a constant flow of argon was maintained over the top of the solution during the experiment. The measurements were conducted at room temperature (20 $\pm$ 2°C).

The electrochemical experiments were performed using a computer-controlled PAR model 173 potentiostat. All data were acquired via a plug-in acquisition board (RC Electronics model IS-16). Customized software was used to record the cyclic voltammograms (CVs) and to perform chronocoulometric experiments and data processing.

3. Results and discussion

3.1. Cyclic voltammetry and differential capacity

Cyclic voltammetry and differential capacities were used for qualitative characterization of the electrode surface.

Fig. 1 shows the cyclic voltammetry curves recorded for the Au(111) electrode in 0.1 M KClO$_4$ solution (dotted curve) and 0.1 M KClO$_4$ + 10^{-3} M KCl (solid curve) over a broad range of electrode potentials that includes the region of gold oxide formation. Adsorption of Cl$^-$ apparently shifts the onset of oxide formation towards more positive potentials and causes a significant distortion of the oxide formation peaks. Insets (a) and (b) in Fig. 1 show the CV and differential capacity curves recorded for potentials restricted to the double-layer region of the gold electrode (before the onset of oxide formation). The shape of these curves is consistent with results reported in the literature [2,3]. The CV and differential capacity curves display a sharp (irreversible) peak at $E \approx 0.2$ V/SCE. This peak can be identified as corresponding to the lifting of the (1 × 23) reconstruction of the Au(111) surface [4,9].

The second (reversible) peak at $E \approx 0.75$ V/SCE corresponds to the formation of an ordered ($p \times \sqrt{3}$) overlayer of adsorbed chloride [4]. The asymmetry of the positive-going and negative-going sections of CVs and the hysteresis in the differential capacity curves indicate that neither the CV nor the differential capacity data correspond to the state of adsorption equilibrium.

Fig. 2 shows a family of charge density curves for 10 KCl concentrations determined from chronocoulometric experiments described in Ref. [1]. The charge densities were measured by waiting at the potential where Cl$^-$ ions are adsorbed for a period of time long enough for the adsorption equilibrium to be established (up to 3 min). Therefore they represent the state of adsorption equilibrium. The charge densities shown in the main section of Fig. 2 represent Cl$^-$ adsorption from 0.1 M KClO$_4$ sup-
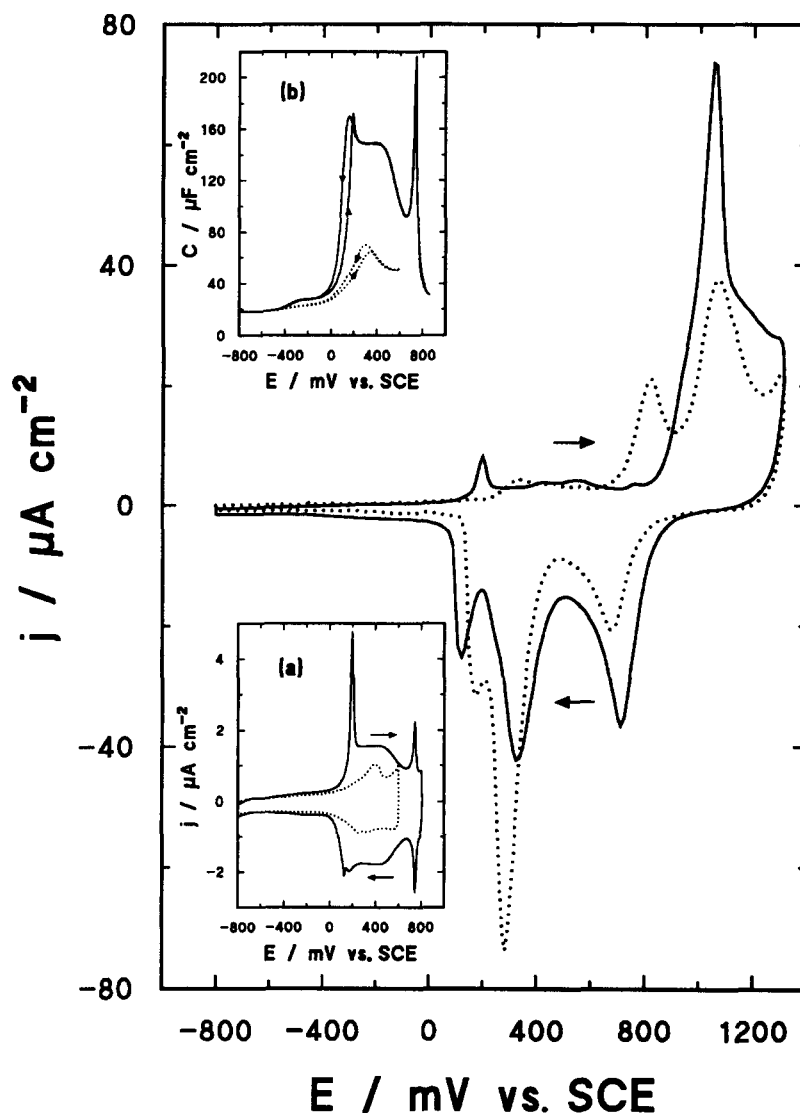

Fig. 1. CV curves recorded at an Au(111) electrode in 0.1 M KClO$_4$ (······) and in 0.1 M KClO$_4$ + 10^{-3} M KCl (———) at a sweep rate of 20 mV s^{-1}. Inset (a) shows the double-layer sections of the CV curves recorded at a sweep rate of 10 mV s^{-1}. Inset (b) shows the corresponding differential capacity curves determined using an ac perturbation of frequency 25 Hz and amplitude 5 mV rms at a sweep rate of 10 mV s^{-1}.
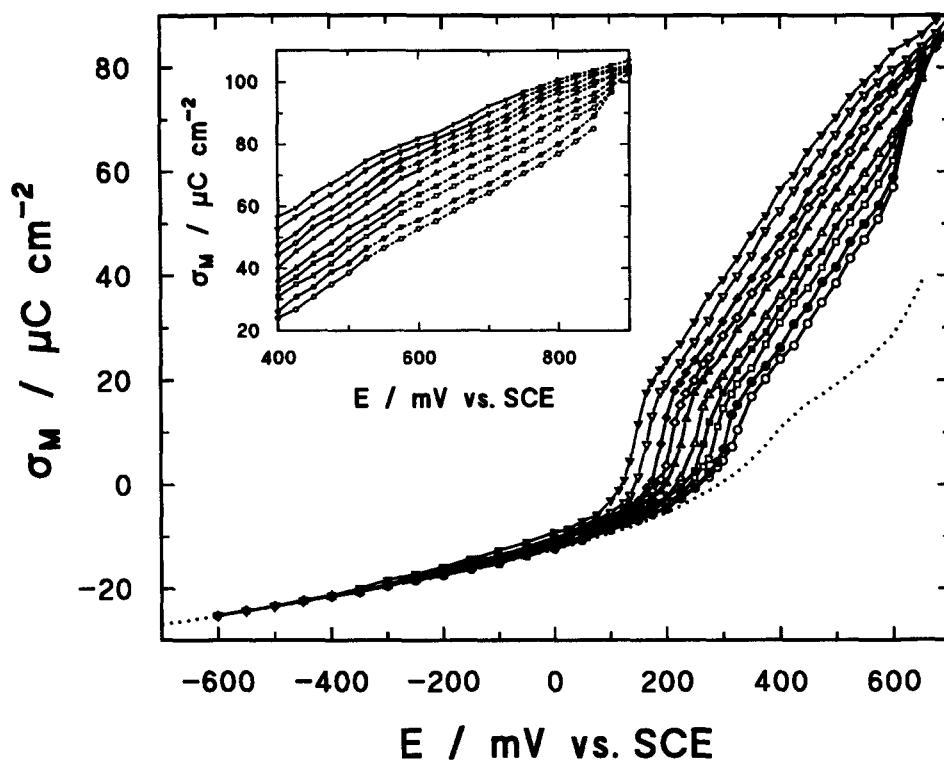
Fig. 2. Charge density versus electrode potential curves for the Au(111) electrode in pure 0.1 M $KClO_4$ solution ($\cdots\cdots$) and with the following KCl concentrations/mol dm^{-3}: $\bigcirc$ 5×10^{-6}; $\bullet$ 10^{-5}; $\square$ 2.5×10^{-5}; $\blacksquare$ 5×10^{-5}; $\triangle$ 10^{-4}; $\blacktriangle$ 2.5×10^{-4}; $\diamond$ 5×10^{-4}; $\blacklozenge$ 10^{-3}; $\triangledown$ 2.5×10^{-3}; $\blacktriangledown$ 5×10^{-3}. The inset to Fig. 2 shows sections of the charge density curves measured for the positive potentials in the acidified electrolyte (0.1 M $KClO_4 + 10^{-3}$ M $HClO_4 + x$ M KCl).
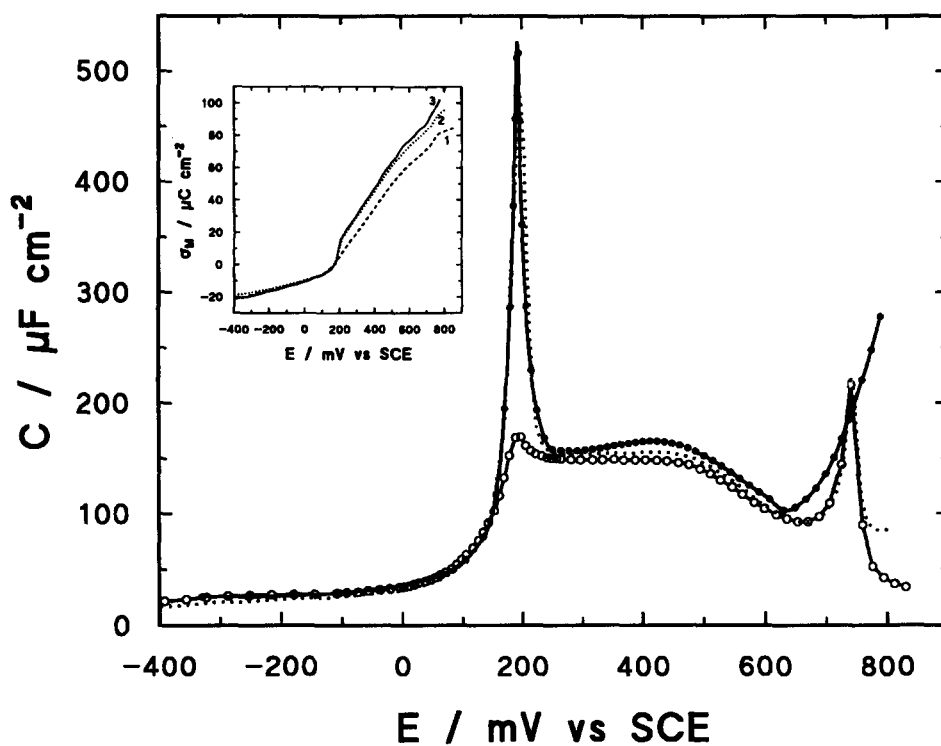

Fig. 3. Differential capacity curves for the Au(111) electrode in 0.1 M $KClO_4 + 10^{-3}$ M KCl solution determined as follows: $\bigcirc$ ac impedance experiment described in Fig. 1(b); $\cdots\cdots$ CV shown in Fig. 1(a); $\bullet$ differentiation of the charge density curve shown in Fig. 2. The inset shows the charge density curves determined as follows: 1, integration of the single-frequency differential capacity; 2, integration of the CV; 3, from chronocoulometry.

porting electrolyte. The inset to Fig. 2 shows sections of the charge density curves measured at more positive potentials in the acidified supporting electrolyte (0.1 M $KClO_4$ + 10^{-3} M $HClO_4$). Adsorption of Cl^- apparently causes a positive charge to flow to the metal side of the interface. The charge density plots measured in the presence of Cl^- can be seen to be composed of several sections. The first is seen at $E < 0.1$ V/SCE and is characterized by a very small slope. The position of the second fast rising segment of the curve correlates well with the position of the sharp peak on CV. The next section, of somewhat smaller slope, corresponds to the potentials of the broad voltammetric peak. The last section is seen at the most positive poten-

tials. It contains a small step whose position correlates with the position of the second reversible peak on CV. The charge densities display a tendency to rise more steeply at the most positive potentials for lower Cl^- concentrations, indicating that gold oxidation/corrosion may overlap with Cl^- adsorption at $E > 0.6$ V.

In Fig. 3, the differential capacity determined from the ac impedance measurement is compared with the capacity calculated from the positive-going section of CV and the capacity calculated by differentiation of charge density data determined from chronocoulometric experiments. The directly measured single-frequency differential capacity is much lower than the capacities determined by the two
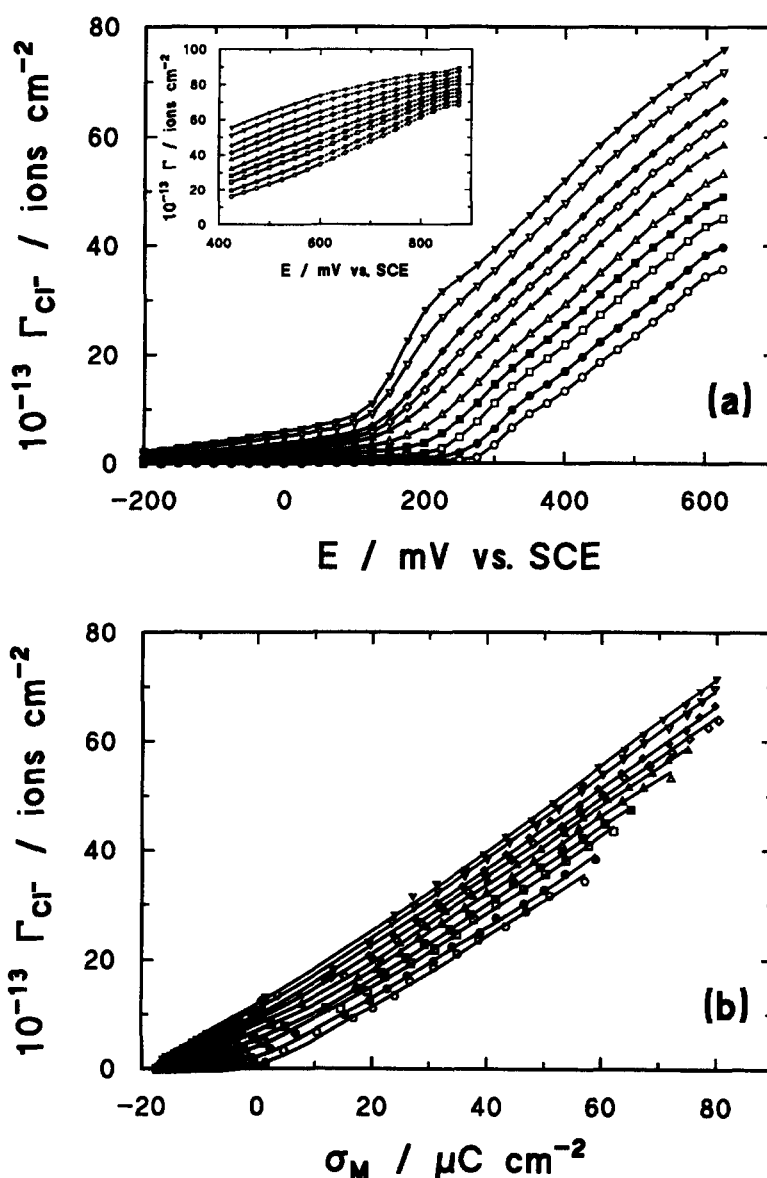

Fig. 4. Plots of the Gibbs excess of Cl^- against (a) electrode potential and (b) electrode charge density for 0.1 M $KClO_4$ with the following KCl concentrations/mol dm^{-3}: ○ 5×10^{-6}; ● 10^{-5}; □ 2.5×10^{-5}; ■ 5×10^{-5}; △ 10^{-4}; ▲ 2.5×10^{-4}; ◇ 5×10^{-4}; ◆ 10^{-3}; ▽ 2.5×10^{-3}; ▼ 5×10^{-3}. The inset to (a) shows the Gibbs excess versus potential plots (dashed lines) determined in 0.1 M $KClO_4$ + 10^{-3} M $HClO_4$ + x M KCl with the same KCl concentrations.

other techniques, particularly in the region of the first large peak (at $E \approx 0.2$ V/SCE). The differences between the capacities determined from CV and by differentiation of the charge densities are less pronounced. The chronocoulometric data reproduce poorly the second differential capacity peak seen at $E \approx 0.75$ V/SCE. In contrast, the capacities calculated from CV and ac impedance measurements give identical results. This behavior confirms that in neutral solutions, for $E > 0.6$ V/SCE, the charge densities determined from chronocoulometric experiments may be affected by the onset of gold oxidation. The inset to Fig. 3 shows that the charge densities determined using ac impedance or cyclic voltammetry are systematically smaller than charge densities determined by chronocoulometry. For this reason further quantitative data analysis was based on the data derived from chronocoulometric experiments. Most of the data analysis will be restricted to $E < 0.6$ V/SCE.

3.2. Gibbs excess data

In this work, the adsorption of Cl$^-$ took place from a solution with an excess of supporting electrolyte. The electrocapillary equation for a gold electrode in contact with that electrolyte is given by [5]

$$-d\gamma = \sigma_M\, dE + \Gamma_{Cl}\text{-}RT\, d\ln c_{KCl} \tag{1}$$

where γ is the interfacial tension, E is the electrode potential measured with respect to SCE and Γ_{Cl}- is the Gibbs excess of Cl$^-$ ions. In order to calculate the Gibbs excess of Cl$^-$ the charge density curves in Fig. 2 were integrated to give relative interfacial tension plots. Next, the relative interfacial tension at constant E was plotted versus ln c_{KCl} and the resulting curves were differentiated to give Γ_{Cl}-. Independently, the Gibbs excess at constant charge was calculated by plotting the Parsons function $\xi = \sigma_M E + \gamma$ [10] and differentiating the relative ξ versus ln c_{KCl} plots at constant σ_M.

Fig. 4(a) shows the plots of Gibbs excess versus electrode potential determined using E as the independent electrical variable. The Gibbs excess plots show three characteristic sections within which the coverage changes with potential in a quasi-linear fashion. The first section is seen at the most negative potentials. It corresponds to low coverages and is characterized by a very small slope. The second section at intermediate coverages is steep. It is followed by a third section with a smaller slope. The inset to Fig. 4(a) shows that the surface concentration versus potential curve levels off further at $E > 0.75$ V/SCE where the ordered ($p \times \sqrt{3}$) overlayer is formed. The thermodynamic data indicate that the transition from the mobile to the ordered state of the overlayer seen at $E \approx 0.75$ V/SCE takes place without a significant change in the surface concentration of Cl$^-$. The maximum surface

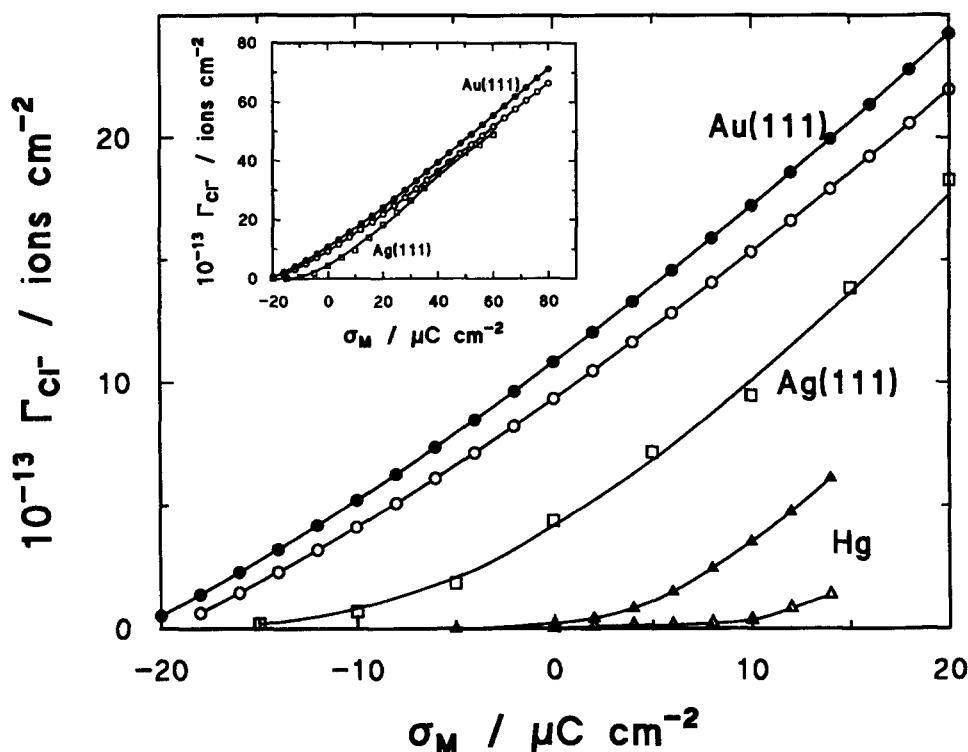Fig. 5. Gibbs excess versus charge density plots for the Au(111) electrode in 0.1 M KClO$_4$ + 10^{-3} M KCl (O) and 0.1 M KClO$_4$ + 5 × 10^{-3} M KCl (●) from this work, for a Ag(111) electrode in x M NaCl + (0.04 − x) M NaF with 0.005 ≤ x ≤ 0.04 from Ref. [11] (□) and for a mercury electrode in x M KCl + (1 − x) M KF (△ x = 10^{-3}; ▲ x = 10^{-2}) from Ref. [12]. The main section shows data for Γ_{Cl}-< 3 × 10^{14} ions cm^{-2}. The inset shows the whole range of surface concentrations measured for gold and silver electrodes.
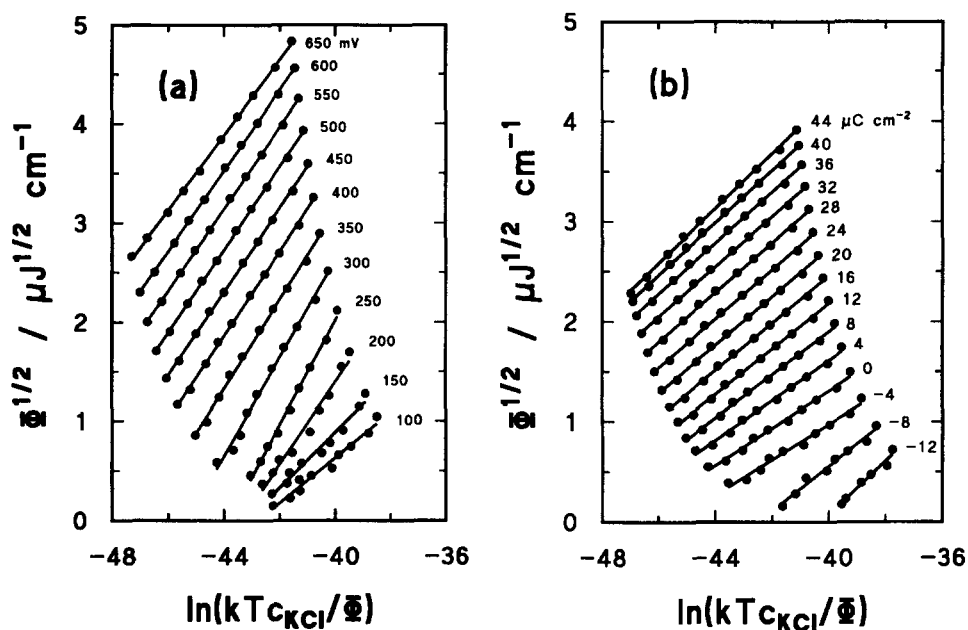
Fig. 6. Fit of the adsorption data to the equation for the square root isotherm at (a) constant potential and (b) constant σ_M.

concentration of Cl^- that was measured for the most positive potential (0.9 V/SCE) and the highest bulk KCl concentration (5×10^{-3} M) employed in this work corresponds to 9×10^{14} ions cm^{-2}. This number is equal to the maximum packing density in a close-packed hexagonal monolayer of Cl^- calculated assuming that the ionic radius (van der Waals radius) of Cl^- is equal to 1.8 Å. This result

indicates that Cl^- attains very high coverages at the Au(111) electrode surface.

Fig. 4(b) shows the Gibbs excess data plotted against the charge density. For $\sigma_M > 0$ all plots are quasi-linear and parallel to each other. Their slopes are equal to the Esin–Markov coefficients which will be discussed later. The data for Gibbs excess at constant charge can be used
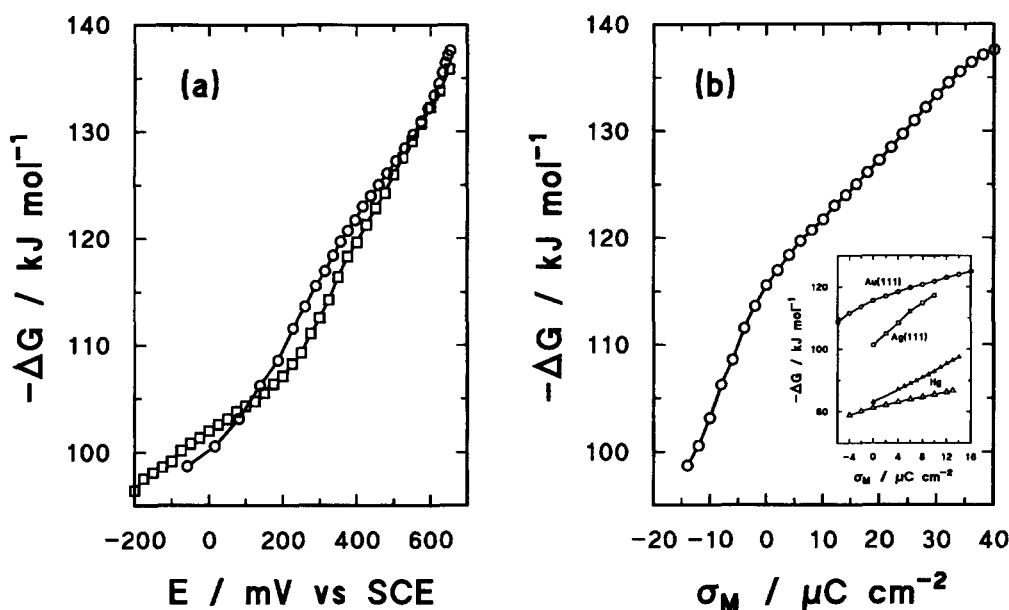

Fig. 7. (a) Plot of the Gibbs energy of adsorption versus electrode potential: □ determined from the $\Phi^{1/2}$ versus $\ln(kTc_{KCl}/\Phi)$ plots at constant E in Fig. 6(a); ○ determined from the $\Phi^{1/2}$ versus $\ln(kTc_{KCl}/\Phi)$ plots at constant σ_M in Fig. 6(b). (b) Plot of the Gibbs energy of adsorption versus electrode charge density determined from the $\Phi^{1/2}$ versus $\ln(kTc_{KCl}/\Phi)$ plots at constant σ_M in Fig. 6(b). The inset shows the Gibbs energy of Cl^- adsorption at Au(111) from this work (○), at Ag(111) calculated from the data in Ref. [11] (□) and at mercury calculated from the data in Ref. [12] (△) and Ref. [14] (▲).

to compare Cl^- adsorption at the Au(111) surface with adsorption of this anion at Ag(111) and mercury electrodes. Fig. 5 shows two Γ_{Cl^-} versus σ_M plots for Au(111) selected from this work compared with the plots determined for a Ag(111) electrode by Valette et al. [11] and for a mercury electrode by Payne [12]. The curves shown in the main section of Fig. 5 are for $\Gamma_{Cl^-} < 3 \times 10^{14}$ ions cm^{-2}, since the data for the mercury electrode were measured for low coverages only. The inset to Fig. 5 shows the whole range of surface coverages that were measured for gold and silver electrodes. The plots in Fig. 5 have comparable slopes for $\Gamma_{Cl^-} > 3 \times 10^{13}$ ions cm^{-2} indicating that the Esin–Markov coefficients have comparable values for Cl^- adsorption at all three metals. These results also show that plots for the Au(111) electrode are strongly shifted along the σ_M axis in the negative direction, indicating that Cl^- adsorption at gold is much stronger than at silver or mercury electrodes. Overall, the position of the Γ_{Cl^-} versus σ_M plots for the three metals on a common graph indicates that the strength of Cl^- adsorption increases in the following order Au(111) > Ag(111) > Hg.

3.3. Gibbs energies of adsorption

To determine the Gibbs energies of adsorption we followed Parsons' suggestion and fitted the surface pressure data Φ to the equation of a "square root" isotherm [11,13]:

$$\ln(kTc_{KCl}) + \ln \beta = \ln \Phi + B \Phi^{1/2} \qquad (2)$$

where $\beta = \exp(-\Delta G/kT)$ is the adsorption equilibrium constant, B is a constant and Φ is the surface pressure. When analysis was carried out at a constant potential, Φ was set equal to $\gamma_{\theta=0} - \gamma_\theta$. In contrast, we used $\Phi = \xi_{\theta=0} - \xi_\theta$ when charge was used as the independent electrical variable. The subscripts θ and $\theta = 0$ denote the values of the interfacial tension and the Parsons function in the presence and absence respectively of Cl^- ions in the supporting electrolyte.

Figs. 6(a) and 6(b) show plots of the square root of the surface pressure versus $\ln(kTc_{KCl}/\Phi)$. The plots are almost linear and when extrapolated to zero surface pressure give the following intercept with the $\ln(kTc_{KCl}/\Phi)$ axis:

$$\lim[\ln(kTc_{KCl}/\Phi)_{\Phi=0}] = -\ln \beta \qquad (3)$$

from which the Gibbs energies of adsorption can be calculated. Note that in Eqs. (2) and (3) the KCl concentrations are multiplied by the term kT so that in the limit of low coverages the film pressure is described by Henry's law $\Phi = kT\beta c_{KCl}$ as explained in Ref. [11]. The Gibbs energies of adsorption, determined using this procedure, are plotted against potential and charge in Figs. 7(a) and 7(b) respectively. The standard state is an "ideal" $\Gamma = 1$ ion cm^{-2} for the adsorbed species and an "ideal" $c_{KCl} = 1$ mol dm^{-3} for the bulk species.

We would like to emphasize that the square root isotherm is an empirical isotherm and, although it is called a "virial type isotherm", Eq. (2) cannot be derived from the equation of state for the virial isotherm [13]. The isotherm is not based on a well-defined physical model and hence should be viewed only as a convenient procedure for linearizing experimental data. Although the fit to the square root isotherm gives linear plots, the extrapolation to zero surface pressure is very long. Consequently, even a small change in the slope may lead to a significant error in the intercept. The constant-charge and constant-potential analyses give plots of a different slope. Therefore it is useful to compare Gibbs energies determined at constant E and constant σ_M to check the consistency of their values. For that purpose the ΔG data determined from the constant charge analysis were also plotted against the electrode potential in Fig. 7(a) together with the ΔG values determined from the constant E analysis. The charge density versus potential curve for the Cl^--free supporting electrolyte was used to convert the Gibbs energy data from ΔG versus σ_M to the ΔG versus E scale. The agreement between ΔG values determined from the constant-charge and constant-potential analyses is very good and indicates that the Gibbs energy data are free from major errors owing to the long extrapolation procedure that was used.

The Gibbs energy plots are nonlinear and can be formally decomposed into three segments of different slopes corresponding to negatively charged surface, moderate positive charge densities $(0 < \sigma_M < 30 \ \mu C \ cm^{-2})$ and high charge densities $(\sigma_M > 30 \ \mu C \ cm^{-2})$ respectively. This behavior reflects a multistate character of Cl^- adsorption at the Au(111) surface. It is also useful to note that the ΔG versus E plot is concave while the ΔG versus σ_M curve is convex. The Gibbs energies of adsorption determined for the Au(111) electrode in this work are compared with the data for the Ag(111) surface obtained by Valette et al. [11] as well as with the results obtained for the mercury electrode by Payne [12] and Hurwitz et al. [14] in the inset to Fig. 7(b). The comparison shows that Cl^- adsorption at gold is significantly stronger than at the other two metals in the whole range of charge densities investigated. The shape and slope of ΔG versus σ_M plots change with the nature of the metal. The plots for gold and silver electrodes are convex, while the plots for mercury are almost linear. These properties indicate that Cl^- adsorption at the group IB metals and at mercury has a somewhat different character.

3.4. Electrosorption valency

The first derivative of ΔG versus E is equal to the electrosorption valency γ'. The electrosorption valency can be determined independently from the slope of the charge density versus Gibbs excess plots:

$$\gamma' = \frac{1}{F}\left(\frac{\partial \Delta G}{\partial E}\right)_\Gamma = -\frac{1}{F}\left(\frac{\partial \sigma_M}{\partial \Gamma}\right)_E \qquad (4)$$
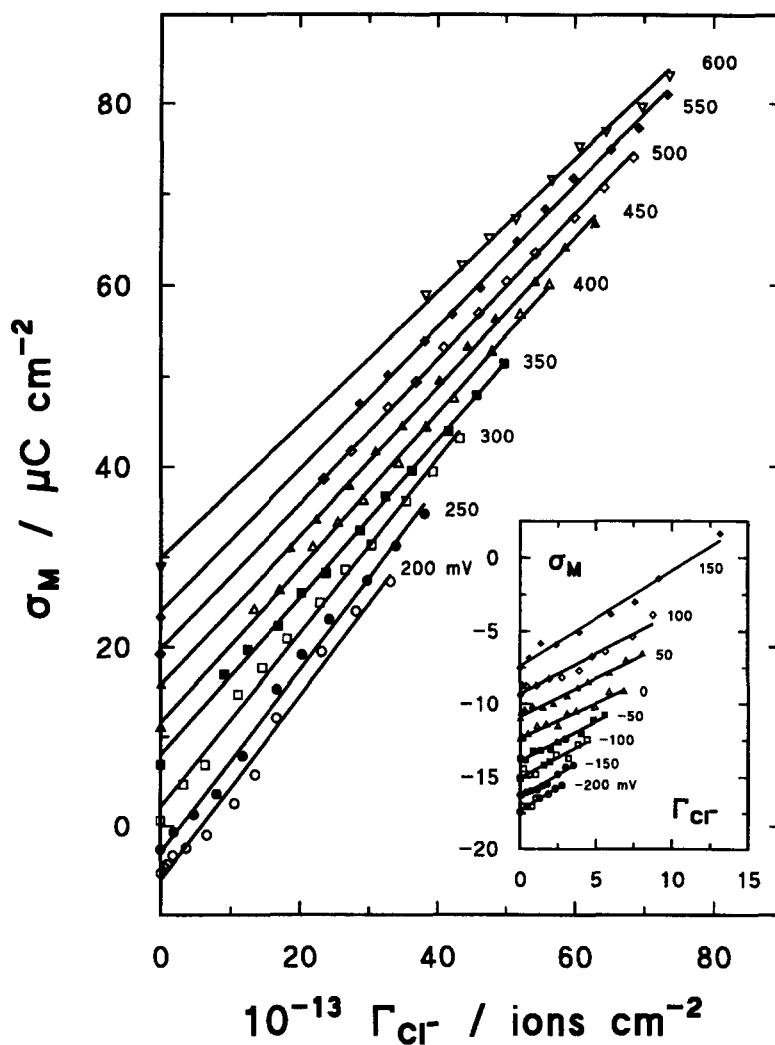
Fig. 8. Plots of the electrode charge density versus Gibbs excess of Cl⁻ taken at constant values of the electrode potentials mV (SCE).

Thus the slope of the σ_M versus Γ_{Cl^-} plots can be compared with the first derivative of the ΔG versus E plot as a further test of the reliability of the ΔG data.

Fig. 8 shows a plot of σ_M versus Γ_{Cl^-} for various electrode potentials. The plots for positive charge densities are shown in the main section of Fig. 8. The plots for negative σ_M are presented in the inset. The data display a linear relation between σ_M and Γ_{Cl^-}. At higher potentials a relatively narrow range of Gibbs excesses was available. However, since the plots included the values of σ_M measured in the pure supporting electrolyte the uncertainty about their slope was somewhat reduced. The electrosorption valencies calculated from the slopes of the σ_M versus Γ_{Cl^-} plots are plotted as a number of electrons flowing to the interface per adsorbed Cl⁻ ion in Fig. 9. In addition, the ΔG values plotted versus E in Fig. 7(a) were fitted to a polynomial and their derivative was determined. The results are also plotted in Fig. 9. Although there are some numerical differences between the values of the electrosorption valency determined by the two procedures, the two γ' versus E plots have a similar shape, indicating that

no major errors were made in the data processing. The electrosorption valencies display a significant dependence on the electrode potential, indicating that the character of
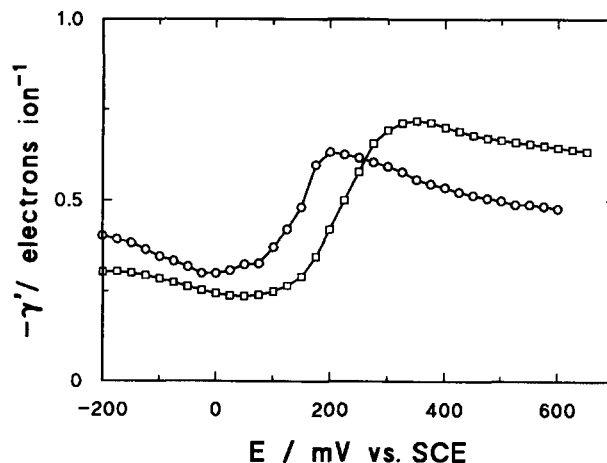

Fig. 9. Electrosorption valencies determined from the slope of the charge versus the Gibbs excess plots (○) and from the Gibbs energy versus electrode potential plots (□).

Cl^- adsorption changes on moving from the negative to the positive end of polarizations investigated. We shall discuss this behavior later after introducing a model of the interface.

3.5. Esin–Markov coefficients

Cross-differentiation of Eq. (1) gives the following expression for the Esin–Markov coefficient:

$$\frac{1}{RT}\left(\frac{\partial E}{\partial \ln c_{KCl}}\right)_{\sigma_M} = -\left(\frac{\partial \Gamma_{Cl^-}}{\partial \sigma_M}\right)_{\ln c_{KCl}} \tag{5}$$

The first derivative in Eq. (5) is given in terms of a directly measured quantity such as σ_M and experimental variables such as potential and bulk KCl concentration. The second derivative is given in terms of the Gibbs excess, a quantity whose calculation involves one integration and one differentiation step. Therefore Eq. (5) can be used to check that no major errors were involved in the calculation of Γ_{Cl^-}. Fig. 10(a) shows a plot of E versus $-RT \ln c_{KCl}$ for various electrode charge densities in the range from -5 to 80 μC cm^{-2}. The plots are linear and their slopes give the Esin–Markov coefficients. Independently, The Γ_{Cl^-} versus σ_M plots from Fig. 4(b) were fitted by a polynomial and differentiated numerically to give $(\partial \Gamma_{Cl^-}/\partial \sigma_M)_{\ln c_{KCl}}$. The two independently determined derivatives are plotted against each other in Fig. 10(b). The full points are the experimental data and the dotted line is a line of unit slope. The experimental points scatter randomly around the dotted line indicating that the Γ_{Cl^-} are free from major data-processing errors.

The reciprocal of the Esin–Markov coefficient gives the number of electrons flowing to the interface per adsorbed Cl^- ion at a constant bulk KCl concentration. It is interest-

ing to compare this quantity with the electrosorption valency (the number of electrons flowing to the interface per adsorbed Cl^- ion at a constant potential). For this purpose it is useful to recall that Cl^- adsorption can be described by a generalized adsorption isotherm of the form

$$\beta c_{KCl} = f(\Gamma_{Cl^-}) \tag{6}$$

where β is the equilibrium constant defined earlier. Eq. (6) can be differentiated to give

$$RT\left(\frac{\partial \ln c_{KCl}}{\partial E}\right)_{\sigma_M} = \left(\frac{\partial \Delta G}{\partial E}\right)_{\Gamma=0} + RT\left[\frac{\partial f(\Gamma_{Cl^-})}{\partial E}\right]_{\sigma_M} \tag{7}$$

Eqs. (4) and (7) show that the reciprocal of the Esin–Markov coefficient may be equal to the electrosorption valency when the second term on the right-hand side of Eq. (7) is negligible. Fig. 4(b) shows that the Γ_{Cl^-} versus σ_M plots are fairly linear and the reciprocal of their slopes is about -0.95 electron ion^{-1}. The absolute value of the reciprocal of the Esin–Markov coefficient is always higher than the absolute value of the electrosorption valency, indicating that the second term in Eq. (7) is never negligible.

3.6. Model of the inner layer

The thermodynamic quantities described in the preceding sections are free from arbitrary assumptions other than that involved in the Gibbs model of the interface. These quantities are very useful phenomenological parameters; however, they tell little about the structure and charge distribution at the interface unless they are interpreted with the help of a physical model. Below we will discuss the thermodynamic data describing Cl^- adsorption at the $Au(111)$ electrode using the Graham–Parsons model of the
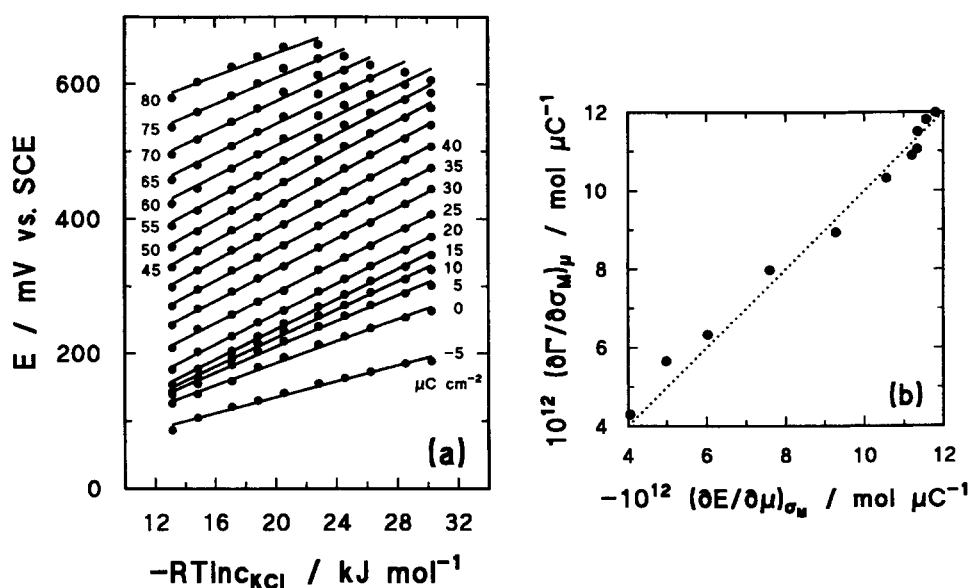

Fig. 10. (a) Esin–Markov plots; (b) comparison of the Esin–Markov coefficients determined from the slope of the E versus $\ln c_{KCl}$ plots in (a) and by differentiation of the Γ_{Cl^-} versus σ_M plots shown in Fig. 4(b).

inner part of the double layer [15]. A total separation of charge at the interface and a specific location for the adsorbed species (inner Helmholtz plane at a distance x_1 from the metal surface) are assumed in this model. We would like to emphasize that the conclusions of this discussion will depend entirely on the validity of the model assumed and this cannot be proved on the basis of electrochemical measurements alone. However, this model has been used to describe a large number of adsorption data. Hence, by using this model we would be able to compare adsorption of Cl^- with adsorption of other ions and to assess the role played by the nature of the metal.

The inner-layer capacity C^i can be calculated from the overall electrode capacity C determined by differentiation of the charge density curves in Fig. 2 and using the theory of the diffuse layer with the help of the formula [11]

$$(C^i)^{-1} = (C)^{-1} - [1 - F(\partial \Gamma_{Cl^-}/\partial \sigma_M)](C^d)^{-1} \qquad (8)$$

where C^d is the capacity of the diffuse layer and $\partial \Gamma_{Cl^-}/\partial \sigma_M$ is the slope of the plots in Fig. 4(b). The inner layer capacities calculated with the help of Eq. (8) are plotted against the charge density on the metal in Fig. 11. To a good approximation their values are independent of the bulk chloride concentration and are equal to the differential capacity of the interface, indicating that the second term on the right-hand side of Eq. (8) is negligible compared with the first term. The inner-layer capacity of gold is compared with the inner-layer capacity of silver and mercury electrodes in the inset to Fig. 11. The inner-layer capacity for gold is much higher than the values of the inner-layer capacities of the two other metals.

The inner-layer capacity is a function of two variables, charge on the metal and the amount of adsorbed anion. Therefore it can be expressed in terms of two components, the inner-layer capacity at a constant charge $_\Gamma C$ and the inner-layer capacity at a constant amount adsorbed $_\sigma C$, as described by the formula [11,17]

$$(C^i)^{-1} = (_\sigma C)^{-1} - F(\partial \Gamma_{Cl^-}/\partial \sigma_M)(_\Gamma C)^{-1} \qquad (9)$$

The capacity $_\Gamma C$ can be determined from the slope of the plot of the potential drop across the inner layer ($\Delta \phi^{M-2} = E - E_{pzc} - \phi_2$) versus the charge $-F\Gamma_{Cl^-}$ of adsorbed chloride at constant σ_M (ϕ_2 is the outer Helmholtz plane potential). These plots are shown in Fig. 12. They display linear sections at higher coverages and an upward deviation from linearity at lower coverages. Hurwitz et al. [14] demonstrated recently that, in the case of anion adsorption from a mixed electrolyte, a deviation from linearity of the plot of $\Delta \phi^{M-2}$ versus the charge of specifically adsorbed anion may be due to coadsorption of the second anion present in the mixed electrolyte. Adsorption of perchlorate at a gold electrode is certainly much weaker than adsorp-
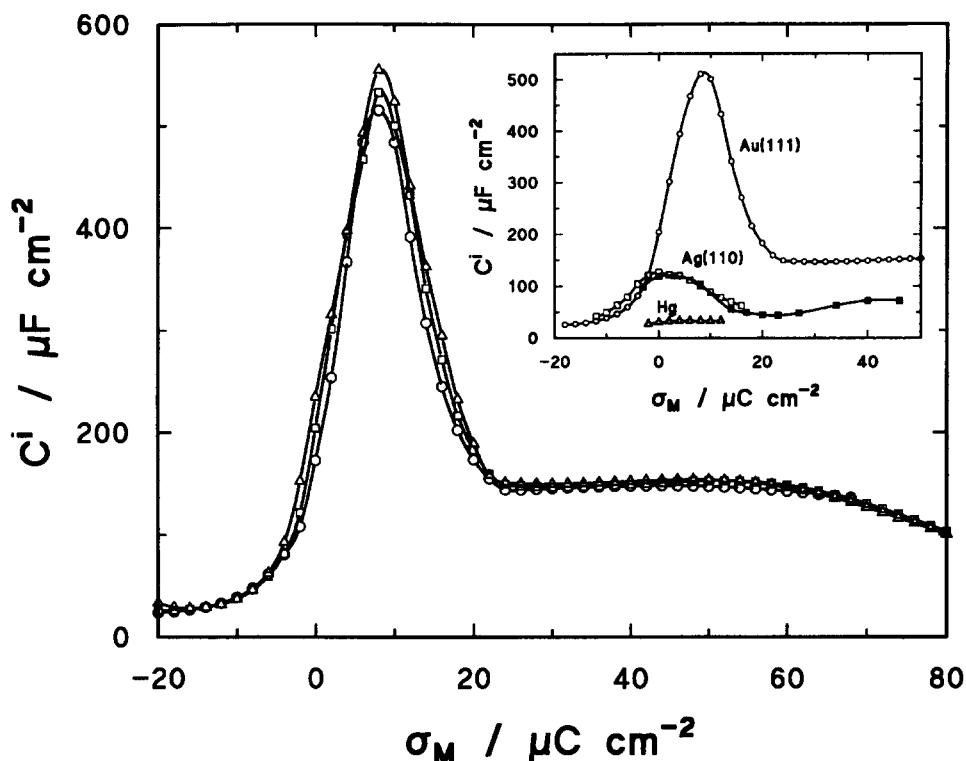

Fig. 11. Inner-layer capacities of the Au(111) electrode in 0.1 M $KClO_4 + x$ M KCl solutions calculated using Eq. (8) for the following KCl concentrations: ○ 2.5×10^{-4} M; □ 10^{-3} M; △ 5×10^{-3} M. The inset shows a comparison of the inner-layer capacities for Au(111) in 0.1 M $KClO_4 + 10^{-3}$ M KCl determined in this work (○), for Ag(110) electrode in x M KCl + (0.02 − x) M KPF_6 with $x = 5 \times 10^{-3}$ [16] (□), for Ag(110) in x M NaCl + (0.04 − x) M NaF with $x = 5 \times 10^{-3}$ [11] (■) and for a mercury electrode in x M KCl + (1 − x) M KF with $x = 10^{-3}$ [12] (△).

tion of Cl^- ion. However, under the experimental conditions used in this work, the bulk perchlorate concentration was always a few orders of magnitude higher than the concentration of Cl^- ion and hence coadsorption of ClO_4^-, particularly at lower values of Γ_{Cl^-}, cannot be entirely ruled out. Consequently, we calculated the inner-layer capacities at constant charge from the linear sections of $\Delta\phi^{M-2}$ versus $-F\Gamma_{Cl^-}$ plots, assuming that the coadsorption of ClO_4^- is negligible at higher Cl^- coverages. The capacities at constant charge can be considered as integral capacities described by the formula

$$_\Gamma C = \varepsilon/(x_2 - x_1) \tag{10}$$

where ε is the permittivity and x_2 the thickness of the inner layer. The capacities at constant amount of adsorbed anion were then calculated from capacities C^i and $_\Gamma C$ using Eq. (9). Independently, $\Delta\phi^{M-2}$ was plotted versus σ_M at a constant amount of adsorbed Cl^- ions, and the $_\sigma C$ capacities were then calculated from the slopes of these plots. The capacities at constant amount adsorbed can also be considered as integral capacities given by

$$_\sigma C = \varepsilon/x_2 \tag{11}$$

Figs. 13(a) and 13(b) show the components of the inner-layer capacity at constant charge and at constant amount adsorbed plotted against the charge density on the metal. The solid line and open circles in Fig. 13(b) indicate capacities calculated from C^i and $_\Gamma C$ using Eq. (9), and the dotted line indicates the capacities determined from the slopes of the $\Delta\phi^{M-2}$ versus σ_M plots. Good agreement between the two sets of data indicates that the computations are free of major errors. The insets to Figs. 13(a) and 13(b) show a comparison of the capacities $_\Gamma C$ and $_\sigma C$ determined for gold in this work and reported for Ag(110) and mercury electrodes in the literature. The adsorption of Cl^- from a mixed electrolyte at silver has been described in two studies [11,16]. The first of these reports Cl^- adsorption in the presence of fluorides, and the second describes Cl^- adsorption in the presence of hexafluorophosphates. The capacities $_\Gamma C$ and $_\sigma C$ calculated from data reported in these two papers are inconsistent. Valette and Parsons [16] suggested that fluorides may coadsorb with chlorides more strongly than hexafluorophosphates and that the results given in their second study are more reliable. Therefore only the data from the second study of
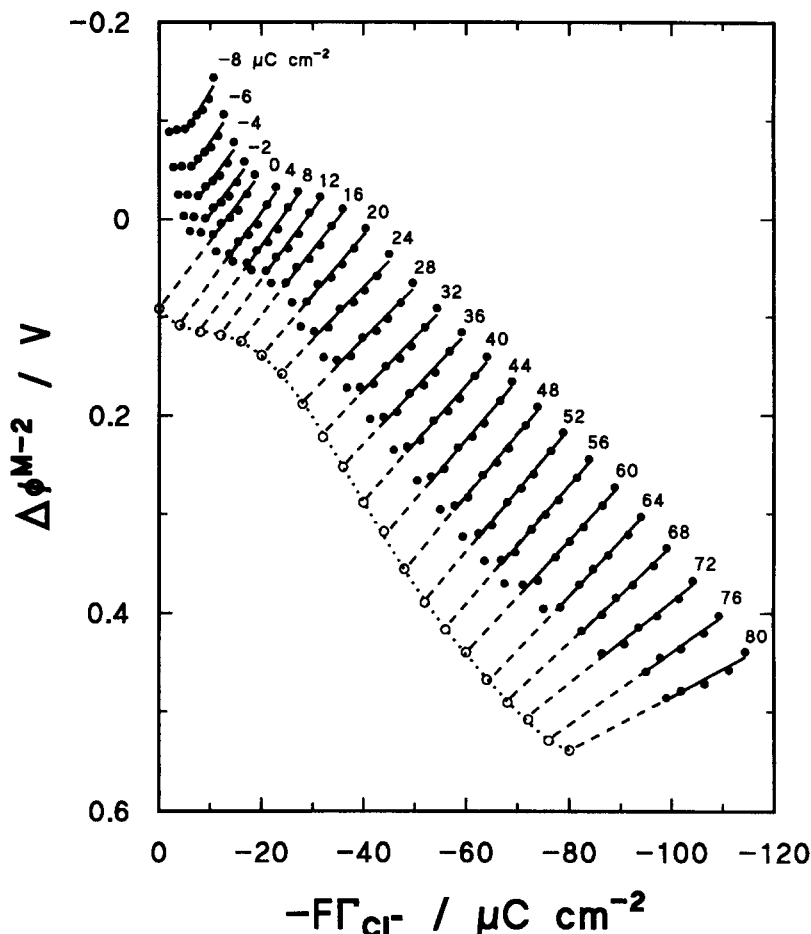

Fig. 12. Plot of the potential drop across the inner layer $\Delta\phi^{M-2}$ versus the charge of adsorbed Cl^- ($-F\Gamma_{Cl^-}$) at constant charge density on the metal side of the interface as indicated in the figure. The dotted lines and open circles represent the potential drop corresponding to the condition of zero diffuse layer charge.

Cl⁻ adsorption on silver are included in insets to Figs. 13(a) and 13(b).

The capacities $_\sigma C$ at constant amount adsorbed display a maximum at small charge densities. The maximum on the $_\sigma C$ curve is usually interpreted as being due to the field induced solvent reorientation and is observed at the charge where the disorientation of water dipoles is at a maximum. The curves for gold and mercury indicate that the maximum solvent disorientation is observed at small positive charge densities. In contrast, the data for silver give a curve with the maximum at small negative charge densities. The maximum values of $_\sigma C$ for gold and silver have comparable magnitudes which are much higher than the maximum value of the capacity determined for mercury. The inner-layer capacities at constant charge $_\Gamma C$ are higher for silver than for gold. The capacities for the two group IB metals are higher than that for mercury. The

interpretation of this $_\Gamma C$ is less straightforward since its magnitude depends not only on the orientation of solvent dipoles but also on how the structure of the inner layer is affected by adsorbed anions.

The ratio of the inner-layer capacities at a constant amount of adsorbed anion and a constant charge is equal to the electrosorption valency [15]:

$$\gamma' = z_\sigma C/_\Gamma C = z(x_2 - x_1)/x_2 \tag{12}$$

Electrosorption valencies determined from the inner-layer capacities using Eq. (12) are shown in Fig. 14. For comparison, the electrosorption valencies, shown earlier in Fig. 9, are replotted against the charge in Fig. 14 (the charge density versus potential curve for the Cl⁻ free solution was used to convert the electrosorption valencies from γ' versus E to the γ' versus σ_M scale). Satisfactory agreement between the electrosorption valencies calculated by
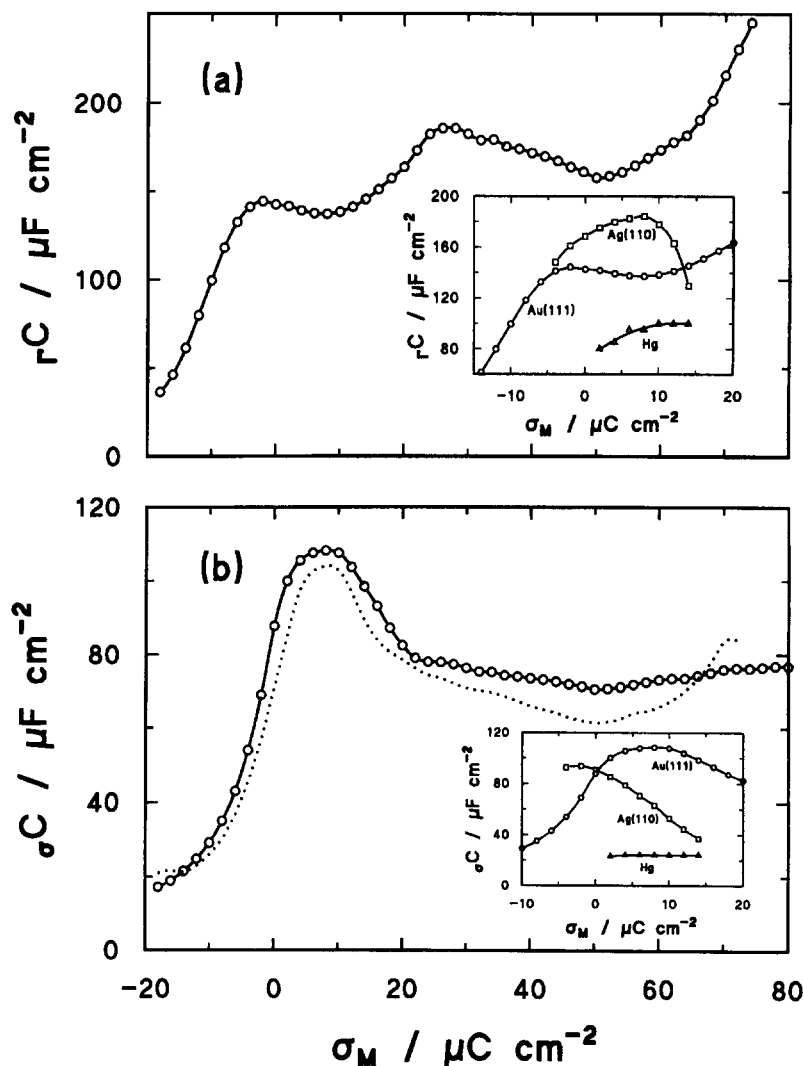

Fig. 13. (a) The component of the inner-layer capacity at constant charge determined from the slope of the $\Delta\phi^{M-2}$ versus $-F\Gamma_{Cl^-}$ plots in Fig. 12. (b) The component of the inner-layer capacity at constant amount adsorbed calculated from the values of C^i and $_\Gamma C$ using Eq. (9) (○) and from the slopes of the $\Delta\phi^{M-2}$ versus σ_M plots (······). The insets show a comparison of the components of the inner-layer capacities at constant amount adsorbed for the Au(111) electrode from this work (○), for the Ag(110) electrode [16] (□) and for the mercury electrode [14] (△).
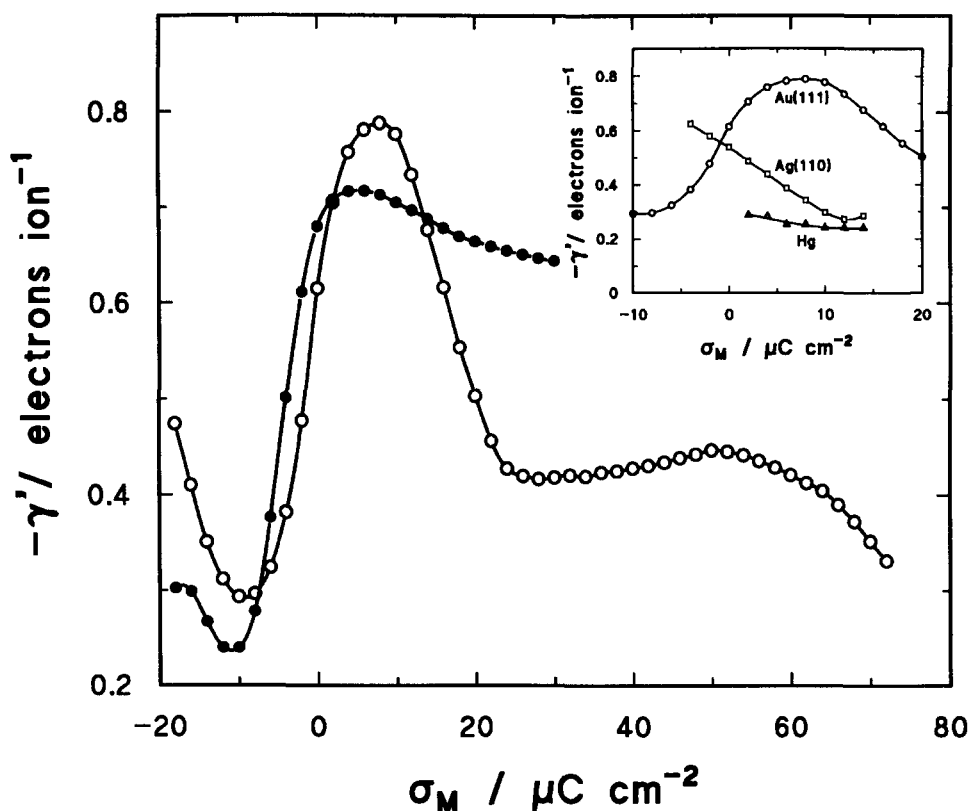
Fig. 14. Plots of electrosorption valency determined from the Gibbs energy versus electrode potential plots (●) and from the ratio of $_\sigma C$ to $_\Gamma C$ (○) against the electrode charge density. The inset shows a comparison of the electrosorption valencies determined for the Au(111) electrode in this work (○), for Ag(110) calculated from the data of Ref. [16] (□) and for mercury plotted from the data of Ref. [14] (△).
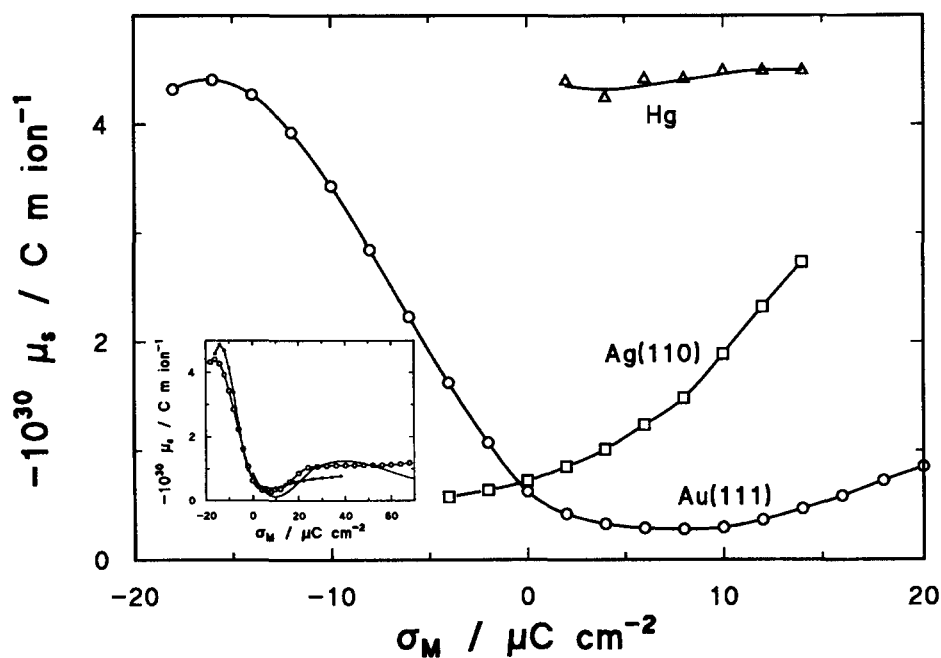

Fig. 15. Plots of the effective dipole moment formed by Cl⁻ ion adsorbed at the metal surface versus the charge density on the metal for Au(111) determined in this work (○), for Ag(110) calculated from the data of Valette and Parsons [16] (□) and for the mercury electrode calculated from the data of Hurwitz et al. [14] (△). The inset shows the change in the effective dipole moment with the charge density for Au(111) determined in this work (————), calculated from the $\Delta\phi^{M-2}$ versus $-F\Gamma_{Cl^-}$ plot under conditions of zero diffuse layer charge (●) and calculated from electrosorption valencies γ' and $_\sigma C$ using Eq. (13) (○). The symbols for the dipole moment are the same as the symbols used to distinguish the corresponding electrosorption valency curves in Fig. 14.

the two methods indicates that no major errors were made in the data processing. The electrosorption valencies determined for Cl^- adsorption at the gold electrode in this work are compared with the electrosorption valencies for Cl^- adsorption at silver and mercury electrodes in the inset to Fig. 14. It should be noted that the electrosorption valencies for gold and silver are strongly dependent on the charge on the metal. At positive charge densities the electrosorption valencies for gold are systematically higher than the values of γ' for silver. The electrosorption valencies for gold are also much higher than the electrosorption valencies for mercury.

The magnitude of the electrosorption valency and its dependence on charge can be discussed in terms of the thickness ratio as described by Eq. (12). However, Parsons and coworkers [18–20] and Schmickler and Guidelli [21–24] have demonstrated that it is better to convert the electrosorption valency into the values of the surface dipole μ_s, which represents a dipole formed by the adsorbed anion and its image charge in the metal, using the formula [19]

$$\mu_s = \frac{ze_0\varepsilon(1 - \gamma'/z)}{_\sigma C} \tag{13}$$

and to discuss the magnitude and the changes of the surface dipole. The advantage of this approach is that the magnitude of the surface dipole is a direct measure of the polarity of the bond formed between the adsorbed anion and the metal. In addition, adsorption from solution is then described in a similar way to adsorption from the gas phase. A comparison of adsorption at the two interfaces becomes quite straightforward in that case. The dipole μ_s can be determined independently by extrapolating the linear segments of the $\Delta\phi^{M-2}$ versus $-F\Gamma_{Cl^-}$ plots in Fig. 12 to the point where the absolute value of the charge of the adsorbed anion is equal to the charge on the metal. At that point the diffuse layer vanishes and the potential drop across the interface takes place within the inner layer. It is then given by

$$\Delta\phi^{M-2} = -\Gamma\mu_s/\varepsilon \tag{14}$$

The extrapolated values of $\Delta\phi^{M-2}$ are shown as open circles and their dependence on the amount of adsorbed anion is shown by dotted lines in Fig. 12. This curve was fitted by a polynomial and differentiated to give the surface dipole μ_s. A comparison of the surface dipole calculated from the electrosorption valencies and from the potential drop across the interface is shown in the inset to Fig. 15. The permittivity of the inner layer was taken as equal to the permittivity of vacuum ($\varepsilon_0 = 8.85 \times 10^{-12}$ $C^2 J^{-1} m^{-1}$) in these calculations. Overall, the agreement between the values of the dipole moment calculated by the two methods is good. Small differences between the two curves seen at charges higher than 20 μC cm^{-2}, and particularly the presence of a maximum on the curve for dipole moments calculated from the potential drop across

the interface, may be an artifact due to the long extrapolation and polynomial fitting procedures used in these computations. The main section of Fig. 15 shows the region of -20 μC $cm^{-2} < \sigma_M < 20$ μC cm^{-2} where the most dramatic changes in the dipole moment take place. For the purpose of further discussion, the surface dipoles for Cl^- at gold are compared with surface dipoles for Cl^- at silver and mercury in this range of charge densities.

Fig. 15 shows that the polarity of the chemisorption bond at gold is large at the negatively charged surface and small at the positively charged surface. The surface dipoles at gold, and also at silver, display quite a significant variation as a function of the electrode charge density. A brief comparison of the curves in Figs. 15 and 13(b) shows that the change of the surface dipole with charge correlates well with the variation of the reciprocal of the inner-layer capacity at constant amount adsorbed. High values of the surface dipole at gold at negative charges correlate well with the small values of the inner-layer capacity. The minimum on the μ_s versus σ_M plot is observed at charges where the $_\sigma C$ curve has a maximum, and a weak dependence of μ_s on charge for $\sigma_M > 20$ μC cm^{-2} corresponds to an essentially constant value of $_\sigma C$ in this range of charge densities. Further, the dipole moment for mercury is independent of charge and this correlates well with the lack of charge dependence of the inner-layer capacity. Finally, the dipole moment for silver has a small value at charges at which the capacity is large and increases at charges at which the capacity drops down.

All dipole moments reported in Fig. 15 are significantly smaller than the value of -8.69 D (1 D $= 3.336 \times 10^{-30}$ C m) for a dipole formed by a charged sphere of ionic radius r_1 adsorbed on a perfect conductor (equal to the product $-e_0 r_1$). Further, at positive charge densities the surface dipole at gold is smaller than the surface dipole at silver and is much smaller than the surface dipole at mercury. The minimum value of the surface dipole at gold is approximately -0.04 D. This can be compared with the minimum value of the dipole for Cl^- adsorbed at mercury and Ag(110) surfaces, which are approximately -1.25 D and -0.18 D respectively. These data indicate that the dipole formed by the adsorbed Cl^- ion and its image charge in the metal is significantly screened by the solvent and the metal, and that the screening is much stronger at gold than at the silver and mercury electrode surfaces. We reported a similar trend for the values of surface dipole formed by sulfate ion adsorbed at these metals [6]. Schmickler and Guidelli [21] described the screening as a combination of the spill-over of electrons from the metal and the polarization of the surface solvent molecules. The spill-over shortens the ion image distance and the dipoles of the solvent screen the dipole of the adsorbate by assuming an orientation opposite to that of the adsorbate dipole. For the zero charge at the metal, they proposed a formula for the dipole moment of an adsorbate in which the screening by the metal is estimated from the jellium model

and the screening by the surface solvent molecules is estimated using the inner-layer capacity. When applied to the case of Cl^- adsorption at gold, the model predicts a very strong screening of the surface dipole to the effect that the predicted dipole of an adsorbate is essentially equal to zero [21–23]. This prediction is in very good agreement with the small value of the surface dipole determined in the present work. We would like to emphasize that in the present work we have described the screening properties of the inner layer not only at the point of zero charge but in a very broad range of charge densities from -20 to $+70$ μC cm^{-2}. Therefore the existing theory can be extended for charges other than zero and tested using these data. Of all the metals gold provides the best opportunity to study ionic adsorption in the broadest range of electrode charge densities and electrode coverages. Therefore the data acquired at gold constitute the best test for the existing theories of the double layer and a challenge for their further refinement.

4. Conclusions

We have performed a thermodynamic analysis of charge density data for adsorption of Cl^- at the Au(111) electrode surface to determine the Gibbs excess, the Gibbs energy of adsorption, the electrosorption valency, the Esin–Markov coefficient and the dipole formed by the adsorbed ion and its image charge on the metal. We have compared thermodynamic data determined in this work with the results for Cl^- adsorption at mercury and silver electrodes reported in the literature.

Of all the metals investigated, gold provides the best opportunity for studying Cl^- adsorption in the broadest range of electrode charge densities and surface concentrations. Adsorption of Cl^- at gold is much stronger than at silver or mercury electrodes. The Cl^- ion forms a polar chemisorption bond with the metal surface whose polarity is a strong function of the charge on the metal. At gold the bond is quite polar at the negatively charged surface; however, its polarity drops significantly at positive charges. Therefore the adsorption behavior of this anion is quite asymmetric with respect to charge on the metal. We have shown that the change in the bond polarity is determined by the ability of the free electrons in the metal and surface solvent molecules to screen the dipole formed by the

adsorbed anion and its image charge in the metal. At positive charge densities, the polarity of the Cl^-–metal bond is much smaller for gold than for silver and mercury. This behavior indicates that the dipole is screened much more effectively at gold than at the other two metals.

Acknowledgment

References

[1] Z. Shi, S. Wu and J. Lipkowski, J. Electroanal. Chem., 384 (1995) 171.
[2] A. Hamelin and J.P. Bellier, J. Electroanal. Chem., 41 (1973) 179.
[3] D.A. Scherson and D.M. Kolb, J. Electroanal. Chem., 176 (1984) 353.
[4] O.M. Magnussen, B.M. Ocko, R.R. Adzic and J. Wang, Phys. Rev. B, 51 (1995) 5510.
[5] Z. Shi, J. Lipkowski, M. Gamboa, P. Zelenay and A. Wieckowski, J. Electroanal. Chem., 366 (1994) 317.
[6] Z. Shi, J. Lipkowski, S. Mirwald and B. Pettinger, J. Electroanal. Chem., 396 (1995) 115.
[7] J. Lipkowski and L. Stolberg in J. Lipkowski and P.N. Ross (Eds.), Adsorption of Molecules at Metal Electrodes, VCH, New York, 1992, p. 171.
[8] J. Richer and J. Lipkowski, J. Electrochem. Soc., 133 (1986) 121.
[9] J. Wang, B. Ocko, A.J. Davenport and H.S. Isaacs, Phys. Rev. B, 46 (1992) 10321.
[10] R. Parsons, Proc. R. Soc. London, Ser. A, 261 (1961) 79.
[11] G. Valette, A. Hamelin, R. Parsons, Z. Phys. Chem. NF, 113 (1978) 71.
[12] R. Payne, Trans. Faraday Soc., 64 (1968) 1638.
[13] R. Parsons, Trans. Faraday Soc., 51 (1955) 1518.
[14] H.D. Hurwitz, A. Jenard, B. Bicamumpaka and W. Schmickler, J. Electroanal. Chem., 349 (1993) 49.
[15] D.C. Grahame and R. Parsons, J. Am. Chem. Soc., 83 (1961) 1291.
[16] G. Valette and R. Parsons, J. Electroanal. Chem., 204 (1986) 291.
[17] R. Parsons, Trans. Faraday Soc., 55 (1959) 999.
[18] R. Parsons, Lecture presented at the Spring Meeting of the Electrochemical Society, Boston, MA, 1986.
[19] K. Bange, B. Strachler, J.K. Sass and R. Parsons, J. Electroanal. Chem., 205 (1987) 87.
[20] R. Parsons, Bull. Electrochem., 6 (5) (1990) 566.
[21] W. Schmickler and R. Guidelli, J. Electroanal. Chem., 235 (1987) 387.
[22] W. Schmickler, J. Electroanal. Chem., 249 (1988) 25.
[23] W. Schmickler, Ber. Bunsenges. Phys. Chem., 92 (1988) 1203.
[24] W. Schmickler in J. Lipkowski and P.N. Ross (Eds.), Structure of the Electrified Interface, VCH, New York, 1993.